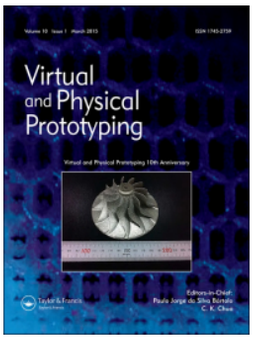

Virtual and Physical Prototyping

ISSN: 1745-2759 (Print) 1745-2767 (Online) Journal homepage: www.tandfonline.com/journals/nvpp20

Single-track investigation of rapid solidification conditions of Hastelloy-X Ni-based superalloy in laser powder-bed fusion and applicability of columnar equiaxed transition criteria

Masayuki Okugawa, Haruki Yoshima , Yuheng Liu, Pan Wang, Yuichiro Koizumi & Takayoshi Nakano

To cite this article: Masayuki Okugawa, Haruki Yoshima , Yuheng Liu, Pan Wang, Yuichiro Koizumi & Takayoshi Nakano (2026) Single-track investigation of rapid solidification conditions of Hastelloy-X Ni-based superalloy in laser powder-bed fusion and applicability of columnar equiaxed transition criteria, Virtual and Physical Prototyping, 21:1, e2639906, DOI: 10.1080/17452759.2026.2639906

To link to this article: https://doi.org/10.1080/17452759.2026.2639906

Published online: 10 Mar 2026.

VIRTUAL AND PHYSICAL PROTOTYPING
2026, VOL. 21, NO. 1, e2639906 (17 pages)
https://doi.org/10.1080/17452759.2026.2639906

Single-track investigation of rapid solidification conditions of Hastelloy-X Ni-based superalloy in laser powder-bed fusion and applicability of columnar equiaxed transition criteria

Masayuki Okugawa [a,b], Haruki Yoshima[a], Yuheng Liu [a], Pan Wang [c], Yuichiro Koizumi [a,b] and Takayoshi Nakano [a,b]

[a]Graduate School of Engineering, The University of Osaka, Osaka, Japan; [b]Anisotropic Design & Manufacturing Research Center, The University of Osaka, Osaka, Japan; [c]Singapore Institute of Manufacturing Technology (SIMTech), Agency for Science, Technology and Research (A*STAR), Republic of Singapore

ABSTRACT

To understand the applicability of the columnar-equiaxed transition (CET) criteria to the rapid cooling conditions unique to the powder-bed fusion (PBF) type additive manufacturing (AM) process, we investigated relationships between the microstructure and the solidification conditions of Hastelloy-X (HX) Ni-based superalloy. Experimental observation revealed columnar crystals are formed in the single-track melt region, and the corresponding computational thermal-fluid dynamics simulations suggest the solidification conditions are mostly out of the range of the solidification conditions conventionally considered for the microstructure controlling: temperature gradient $G = 1.0 \times 10^5$–2.0×10^8 K m^{-1} and solidification rate $R = 1.0 \times 10^{-3}$–4.0×10^0 m s^{-1}. Combining the experimental and computational data, the microstructural morphology of HX was within the range predicted to be columnar crystals in terms of the CET criterion and the parameters obtained by the experiment under conventional solidification conditions. This study sheds light on the applicability of the CET criteria to the PBF process and facilitates the microstructure control of PBF-fabricated structural alloys.

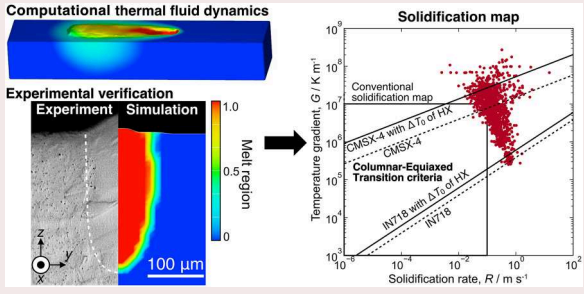

ARTICLE HISTORY
Received 2 April 2025
Accepted 27 February 2026

KEYWORDS
Additive manufacturing; Hastelloy-X nickel-based superalloy; powder bed fusion; selective laser melting; computational thermal-fluid dynamics simulation

1. Introduction

Additive manufacturing (AM) technologies have attracted considerable attention because they facilitate the easy fabrication of three-dimensional (3D) parts with complicated geometry. Among the various AM techniques available, powder bed fusion (PBF) has become the preferred one for metal AM [1–4], in which metal products are built in a layer-by-layer manner using a laser beam or an electron beam to fuse metal powder particles to form objects.

In particular, nickel (Ni) based superalloys fabricated by PBF-type AM have significant applications in the aerospace industry. Weldable superalloys such as IN718 [5–7], IN625 [8, 9] and Hastelloy-X (HX) [10–15] were thoroughly investigated using the PBF-type AM process. In contrast, non-weldable alloys such as IN738LC [16, 17] and CMSX-4 [18, 19], which have superior creep resistance, were considered difficult to fabricate by PBF because of the cracking during the preparation process. Later studies to avoid cracking in PBF have been conducted. Tang et al. [20] suggested a

CONTACT Masayuki Okugawa okugawa@mat.eng.osaka-u.ac.jp 2-1 Yamadaoka, Suita, Osaka 565-0871, Japan; Yuichiro Koizumi ykoizumi@mat.eng.osaka-u.ac.jp 2-1 Yamadaoka, Suita, Osaka 565-0871, Japan

strategy to avoid cracking for fabricating highly reliable AM parts by optimizing the alloy composition. Kontis et al. [14] suggested a strategy to avoid cracking by grain boundary engineering and showed that cracking sensitivities can be reduced by introducing equiaxed grains. Grain refinement is effective not only for obtaining crack-free Ni-based superalloy with high-temperature strength. In general, grain refinement effectively improves the balance of strength and toughness of metallic structural materials. Even for Ni-based superalloys, the condition for obtaining equiaxed-and-fine grains is of great interest in AM of structural alloys. Moreover, grain refinement is of great interest even for non-weldable Ni-based superalloys used as polycrystals, such as HX and IN718.

The microstructures of metals fabricated by the PBF process are solidification microstructures. In general, solidification microstructures can be predicted from solidification conditions defined by the combination of a temperature gradient (G) and solidification rate (R) at a solid/liquid interface, according to the columnar-equiaxed transition (CET) criteria proposed by Hunt [21]. Thus, solidification maps, in which the types of solidification microstructures are indicated in the spaces of G and R, have been proposed as a guide for predicting the microstructure formed by the PBF – AM process toward controlling crystallographic textures via controlling process parameters such as the power, diameter, and scanning speed of the heat source [2, 7, 22–26]. In our previous study, we found that the CET criteria are not applicable to the solidification of 316L stainless steel irradiated with an electron beam [27]. The violation of CET criteria was attributed to the rapid-fluid flow caused by the significant Marangoni effect owing to the large temperature gradient along the surface of the melt surface and the transfer of small crystals which are nucleated in front of the solidification front dendrite. These findings suggest that classical CET frameworks may be insufficient when applied to systems involving strong thermal gradients and beam-induced convection. It is therefore essential to explore whether similar phenomena occur in other alloy systems, particularly under high-energy beam processing conditions.

Melting and solidification in the PBF process occur locally with the length and time scales on the order of millimetres and milliseconds, respectively. This makes the experimental investigation of solidification conditions challenging. An effective approach for investigating solidification conditions in the melt pool involves combining experimental methods with corresponding computer simulations, such as the finite element method and computational thermal-fluid dynamics (CtFD) simulations. Previous studies of stainless steels, Co-Cr-Mo alloy, Ni-based superalloys [15, 27–29] have found that solidification in the PBF processes occurred under significantly high G and R in the ranges of 10^5–10^9 K m^{-1} and 10^{-3}–10^1 m s^{-1}, respectively. These conditions are out of the range of solidification conditions assumed for the conventional solidification map [21]. Indeed, the studies have identified the 'inverse CET' [27, 28]; equiaxed crystalline grains were observed near the outmost part of the melt region, which were solidified under conditions with high flow velocities reaching up to 300 mm s^{-1} induced by the non-uniformity of surface tension arising from the steep temperature gradient along the surface of the melt-pool, i.e. Marangoni flow. These results suggest that equiaxed crystals are formed owing to a high velocity of fluid flow, even though the G and the R are in the range for columnar crystal formation.

In this study, we investigated solidification microstructures of HX induced by laser-beam irradiation. The corresponding solidification conditions at the rapidly migrating solid/liquid interface are also evaluated using a CtFD simulation to examine the applicability of the CET criteria for the PBF-type AM process through comparison with the prediction from well-established physical and metallurgical properties. The relationships between the microstructures and solidification conditions are discussed with reference to the CET criteria for IN718 and CMSX-4 superalloys obtained under conventional solidification conditions. This assessment aims to progress towards controlling the microstructure of alloys fabricated by the PBF-type AM process through comparisons with predictions based on well-established rules for conventional solidification processes, including the CET criteria. In this study, laser irradiation was performed on bulk HX samples without using powder. This approach enables controlled analysis of melt pool formation and solidification behaviour, without the additional complexity introduced by powder packing and particle size variation. While scanning strategies [1, 4] and multi-layer builds [30] are known to affect microstructure formation in the PBF through thermal cycling and heat accumulation. Thus, the knowledge from investigating microstructure formation in single-track scanning is limited and cannot be directly extrapolated to full three-dimensional builds. However, the present study focuses on single-track scanning to establish a fundamental understanding of solidification conditions and grain morphology in isolation under well-controlled thermal conditions. This provides a basis for further extension to multi-layer simulations and scanning path optimisation. Preliminary work on multi-layer modelling has already been initiated [30].

2. Methods

2.1. Laser beam irradiation experiments

For the laser irradiation experiment, we used rolled and recrystallized HX blocks as specimens with dimensions of 20 mm × 50 mm × 10 mm. These were irradiated with a laser beam scanned along straight lines of length 10 mm using a laser AM machine (EOS 290 M). The irradiation was performed with varying beam powers P (180, 240, 300, and 360 W) and scanning speeds V (600, 800, 1000, 1200, and 1400 mm s^{-1}), which are conditions commonly used in AM of Ni-based superalloys [22, 31]. Table 1 lists the line energies for each irradiation condition. The top surfaces of the laser-irradiated samples were observed using a laser microscope (Keyence VK-X200/210) to measure the widths and surface topographies of the melt tracks. The samples were cut perpendicular to the beam scanning direction for cross-sectional observation using field-emission scanning electron microscopy (FE-SEM, JEOL JSM 6500), and the crystal orientation analysis was performed using electron backscatter diffraction (EBSD). The accelerated voltage and the step size of the EBSD analysis were 20 kV and 0.4–0.5 µm, respectively. The size and aspect ratio of each crystal grain were evaluated by analysing the EBSD data. Each irradiation condition was performed once in this study. Cross-sections were taken from the steady-state region of the bead.

2.2. CtFD simulations

CtFD is a computational solution of the equations governing thermo-fluid dynamics, including the conservation laws of mass, momentum, and energy [32, 33]. The CtFD simulations of laser beam irradiation to the HX were performed using commercial 3D thermo-fluid analysis software (Flow Science FLOW-3D® with Flow-3D Weld module) [34]. For the heat source model, a Gaussian heat source model was used, in which the irradiation intensity distribution of the beam is regarded as a symmetrical Gaussian distribution over the entire beam. The beam irradiation intensity distribution is expressed by the following equation.

$$q(r) = \frac{2\eta P}{\pi R^2}\exp\left(-\frac{2r^2}{R^2}\right) \quad (1)$$

Here, P is the power, r is the actual beam radius, and R is the effective beam radius. To make the model even more accurate, the absorption rate η was calculated assuming multiple reflections and incident angle θ dependence based on the Fresnel equation:

$$\eta = 1 - \frac{1}{2}\left\{\frac{1+(1-\varepsilon\cos\theta)^2}{1+(1+\varepsilon\cos\theta)^2} + \frac{\varepsilon^2 - 2\varepsilon\cos\theta + 2\cos^2\theta}{\varepsilon^2 + 2\varepsilon\cos\theta + 2\cos^2\theta}\right\} \quad (2)$$

where ε is the Fresnel coefficient, and η varies with θ as shown in Figure 1.

A local laser melt makes the vaporisation of the material and causes high vapour pressure. This vapour pressure acts as a recoil pressure on the surface, pushing the weld pool down. Reproduce the recoil pressure with the following model

$$p_{\text{recoil}} = Ap_0\exp\left[\frac{\Delta H_{LV}}{RT_V}\left(1-\frac{T_V}{T}\right)\right] \quad (3)$$

Here, ρ_0 is the atmospheric pressure, ΔH_{LV} is the latent heat of vaporisation, R is the gas constant, T_V is the boiling point at the saturated vapour pressure. A is a ratio coefficient that is generally assumed to be 0.54, indicating that the recoil pressure due to evaporation is 54% of the vapour pressure at equilibrium on the liquid surface.

Table 1. Laser-beam irradiation conditions. Four levels of beam power and 5 levels of scanning speed are employed. The values are indicating the line energy (E_{line}/ J mm^{-1}).

		Scanning Speed, V / mm s^{-1}				
Line Energy, E_{line} / J mm^{-1}		600	800	1000	1200	1400
Beam power, P, W	360	0.60	0.45	0.36	0.30	0.26
	300	0.50	0.38	0.30	0.25	0.21
	240	0.40	0.30	0.24	0.20	0.17
	180	0.30	0.23	0.18	0.15	0.13

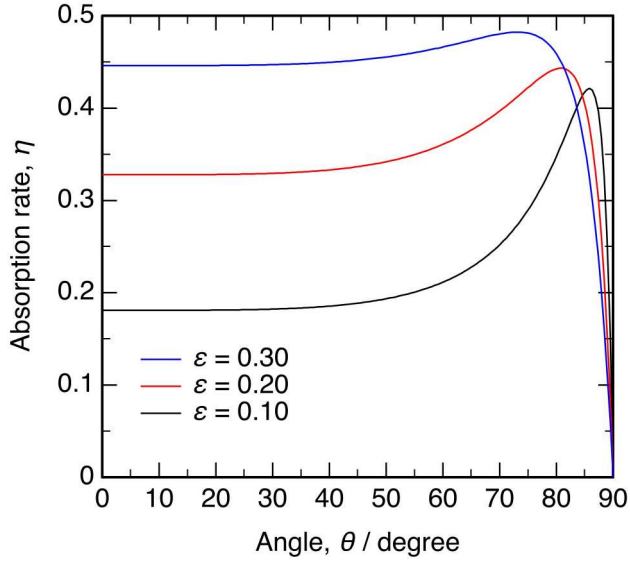

Figure 1. Absorption rate η as a function of incident angle θ.

Table 2. Parameters used in the CtFD simulations. The values at 298.15 K are indicated as a representative for temperature dependent parameters.

Name	Symbol	Value	Ref.
Density at 298.15 K	ρ	8.24 g cm^{-3}	[*]
Liquidus temperature	T_L	1628.15 K	[*]
Solidus temperature	T_S	1533.15 K	[*]
Viscosity at T_L	η	0.0068 kg m^{-1} s^{-1}	[*]
Specific heat at 298.15 K	C_P	0.439 J g^{-1} K^{-1}	[*]
Thermal conductivity at 298.15 K	λ	10.3 W m^{-1} K^{-1}	[*]
Surface tension at T_L	γ_L	1.85 J m^{-2}	[*]
Temperature coefficient of surface tension	$d\gamma_L/dT$	-2.5×10^{-4} J m^{-2} K^{-1}	[*]
Emissivity	E	0.27	[35]
Stefan–Boltzmann constant	σ	5.67×10^{-8} W m^{-2} K^{-4}	[35]
Heat of fusion	ΔH_{SL}	2.76×10^{2} J g^{-1}	[36]
Heat of vaporisation	ΔH_{LV}	4.29×10^{3} J g^{-1}	[36]
Vaporisation temperature	T_V	3110 K	[36]

*Calculated using JMatPro v11.

Table 2 lists the simulation parameters, most of which were evaluated using an alloy physical property calculation software (Sente software JMatPro v11). The emissivity and Stefan – Boltzmann constant values were obtained from Ref. [35], and the values for pure Ni [36] were used for the heat of vaporisation and vaporisation temperature. The dimensions of the computational domain of the numerical model were 4.0 mm in the beam scanning direction, 0.4 mm in width, and 0.3 mm in height. A uniform mesh size of 10 μm was applied to the computational domain. The boundary condition of continuity was applied to all the boundaries except for the top surface. The temperature was initially set to 300 K, and P and V were the same as those used in the experiment. The solidification conditions at the solid/liquid interface, that are, G, R, the cooling rate, and the fluid flow velocity (U), were calculated from the obtained temperature distributions. The relationships between these solidification conditions and microstructures were examined based on the experimental and simulation results.

3. Results and discussion

3.1. Experimental observation of melt pools

Figure 2(a) shows surface laser microscope images and corresponding height maps of the centre parts of single beads formed with various combinations of P and V. The laser beam scanning direction was from the bottom to the top of the image. The surface morphology of a single bead varies depending on the process parameters; for example, uniformly melted beads were formed through laser beam irradiation under (1) low V and (2) high beam power and high V conditions. However, a chain of droplet-like melt tracks was formed under high scanning speed conditions. This phenomenon is similar to the 'balling phenomena' in the PBF-LB process. A discontinuous track was also observed in the melted regions of the IN738LC Ni-based superalloy by laser beam irradiation [37], possibly caused by Rayleigh – Plateau instability, reducing the surface energy by breaking up the continuous liquid cylinder into metallic droplets. Figure 2(b) shows cross-sectional optical microscopy images of the laser-beam melt region of the HX. The fusion line is indicated by the dashed lines. The fusion line corresponds to the melt-pool boundary in parts fabricated by PBF. As the line energy increases, the width of the melt region becomes larger. Similarly, the bead depth increases with increasing P and decreasing scan speed, reflecting the higher energy input and deeper penetration into the substrate.

The width and depth of the melt pools were measured from the surface and cross-sectional images, respectively. Figure 3 shows the width (Figure 3(a)), depth (Figure 3(b)), and aspect ratio (Figure 3(c)) of the melt pools formed by scanning the laser beam as a function of line energy. The width (Figure 3(a)) increased and approached approximately 160 μm as the line energy increased under all the conditions. It is suggested that bulk metal melts at the same bead width at a sufficiently slow speed in the range used in this study. The depth of the melt pools (Figure 3(b)) increased monotonically as the line energy increased, regardless of the changes in P and V. The aspect ratio also increased linearly at the P values of 300 and 360 W. On the other hand, when P was 180 and 240 W, the aspect ratio (Figure 3(c)) tended to saturate at line energies higher than 0.3 J mm^{-1}. According to the conventional studies of laser welding [38], two types of melting mechanisms were considered: (i) conduction-mode melting due to thermal diffusivity and (ii) keyhole-mode melting due to vaporisation of the metal. The preferential melting mode is determined basically by the beam power (P) and scanning speed (V) of the irradiated laser and the resultant line energy defined by $E_{line} = P/V$. The melting mode transition has also been observed in the PBF-LB process of the IN738LC Ni-based superalloy and the melting mode was determined by the threshold P of approximately 210 W [37]. The threshold beam power for the melting mode in this study was estimated to be approximately 240 W, and the similarity of the threshold value suggests that there are two modes of melting mechanisms.

The microstructures of the laser-irradiated regions in the HX samples were investigated using SEM-EBSD. Figure 4 shows the cross-sectional inverse pole figure (IPF) z orientation maps of the melt region. Bright colours indicate the melt regions, which were confirmed with the optical images. Epitaxial growth

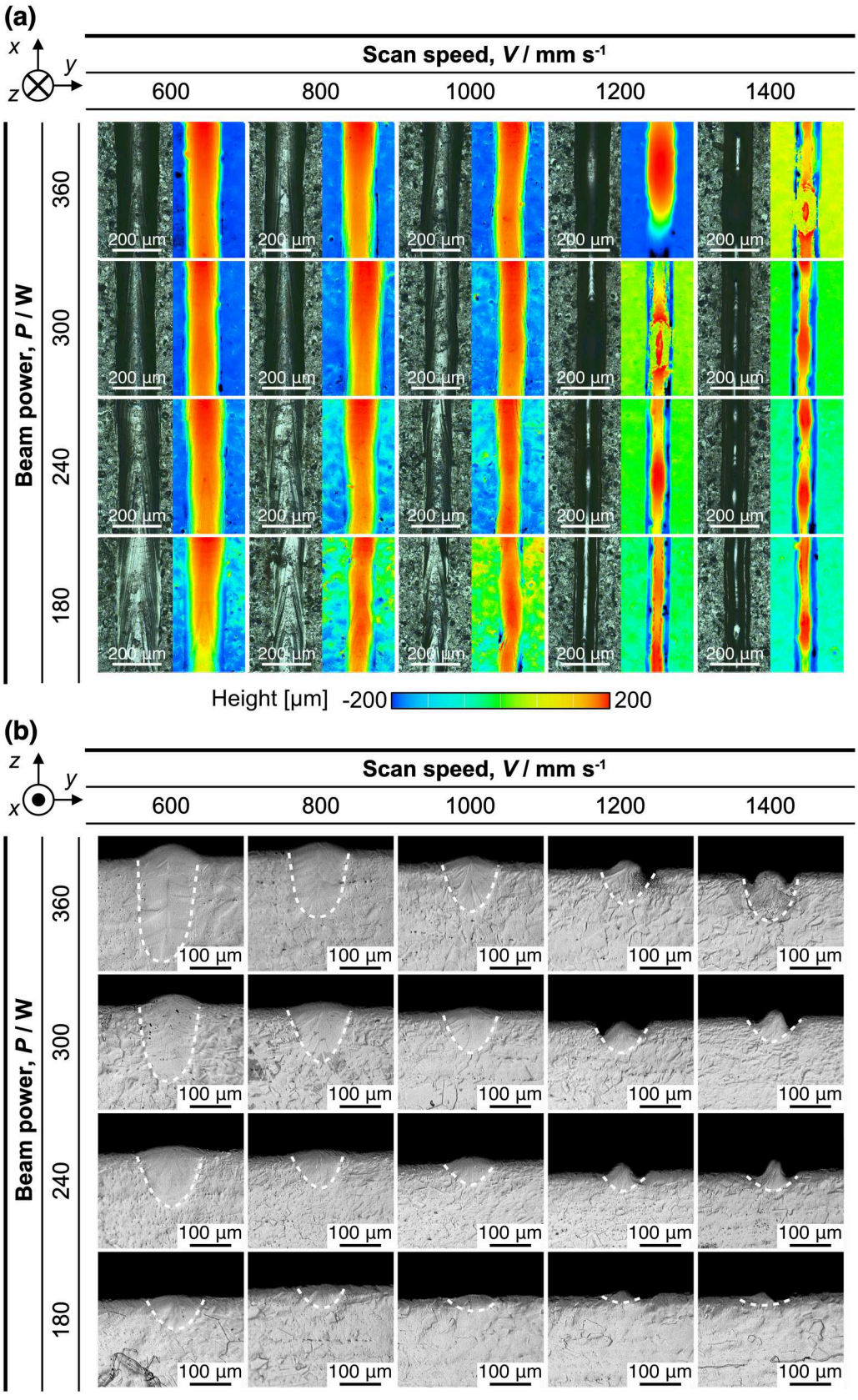

Figure 2. (a) Laser microscope images (left) and corresponding height maps (right) of the top surface of melt-tracks formed by laser irradiation on the HX block under varying condition with four levels of beam power (*P*) and scan speed (*V*). (b) Corresponding cross-sectional optical microscope images of the laser-beam-irradiated region of the HX.

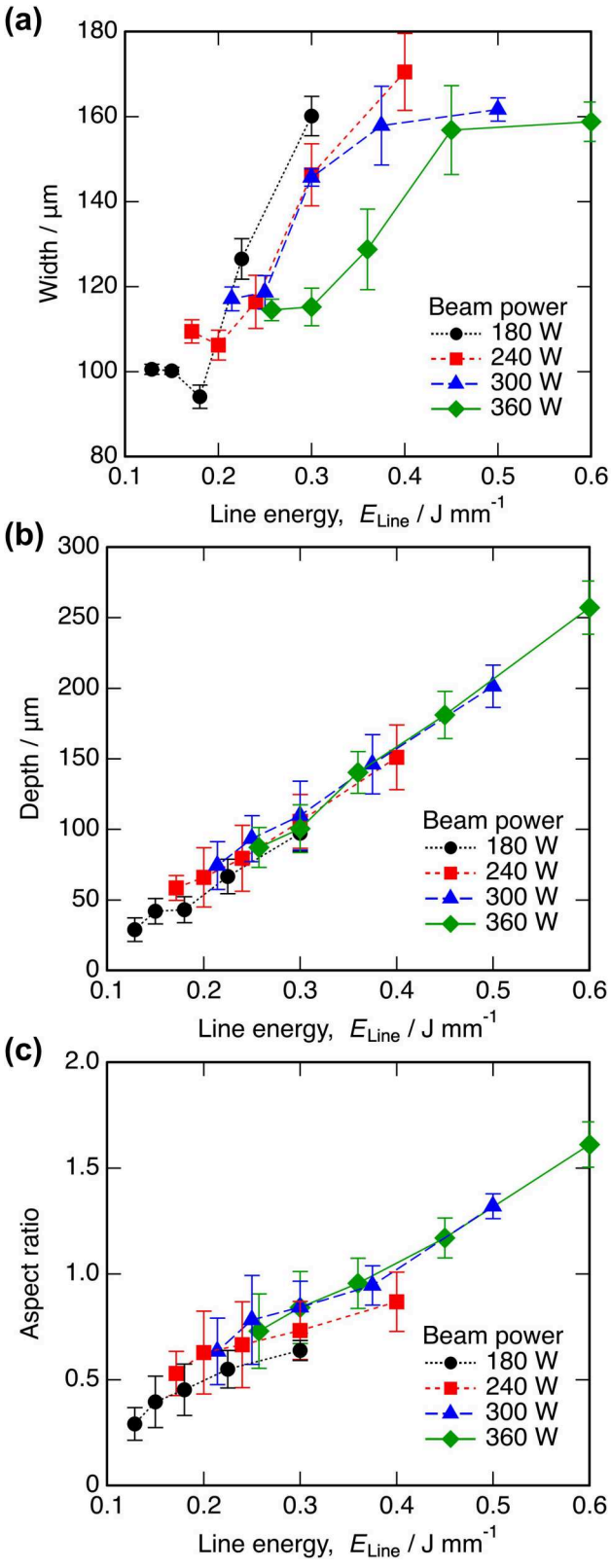

Figure 3. Geometries of the melt region in the HX samples subjected to laser irradiation at various levels of powers (P) and scanning speeds (V) as a function of line energy, $E_{line} = P/V$. (a) Width of melt-region, (b) Depth of melt region, and (c) Ratio of depth to width.

from the non-melted region was observed under all conditions, and columnar crystal grains with diameters of approximately 5–10 μm appeared at the centre of the melt regions. The shallow melt pools were formed at low P and high V, and the crystal grains grew from the boundary between the left and right melt pools. On the other hand, crystal grains growing in the z direction were observed from the lower centre at high P and low V. From these EBSD data, the average grain sizes and their aspect ratios in the melt regions were evaluated. Crystal grains of approximately 5–10 μm in size with an aspect ratio of 2–4 were formed. As shown in Figure 5, the average aspect ratios of the laser-melted regions in the HX samples are not understood in terms of the line energy, and the morphology of the microstructures does not change significantly with the process parameters. The grain size in the material appears to be influenced by the pre-existing grain size in the underlying material rather than the solidification conditions, which depend on the process conditions. The larger the original crystal grains are, the larger the crystal grains in the melt region seem to be, suggesting that the solidification is dominated by epitaxial growth. Although the number of grains in each melt pool enables statistical analysis of grain orientation and morphology, future work will include repeated trials to quantify variability in melt pool dimensions and microstructure.

3.2. CtFD simulations

Figure 6 shows a snapshot of the CtFD simulation of HX where P and V were 360 W and 600 mm s^{-1}, respectively. The melt pool became stable after approximately 2 ms, i.e. travelling approximately 1.2 mm, and eventually, a melt pool with an elongated teardrop shape was formed (Figure 6(a)). The transverse and longitudinal sections of the melt pool coloured by temperature and solid fraction are shown in Figure 6(b1) and Figure 6(b2), respectively. Keyhole-mode melting can be seen at the front of the melt region: the solid metal was melted through laser beam irradiation (Figure 6(c)), and the molten liquid was pressed down to the bottom of the melt pool (Figure 6(d)). As a result, the melt pool is relatively deep, and subsequently, the liquid on both sides of the keyhole joined together (Figure 6(e)) and solidified (Figure 6(f)).

The Fresnel coefficient, which determines beam absorption efficiency, was used as a fitting parameter to reproduce the morphology of the experimentally observed melt region. Figure 7(a) compares a CtFD-simulated melt pool model of HX to the EBSD IPF-z

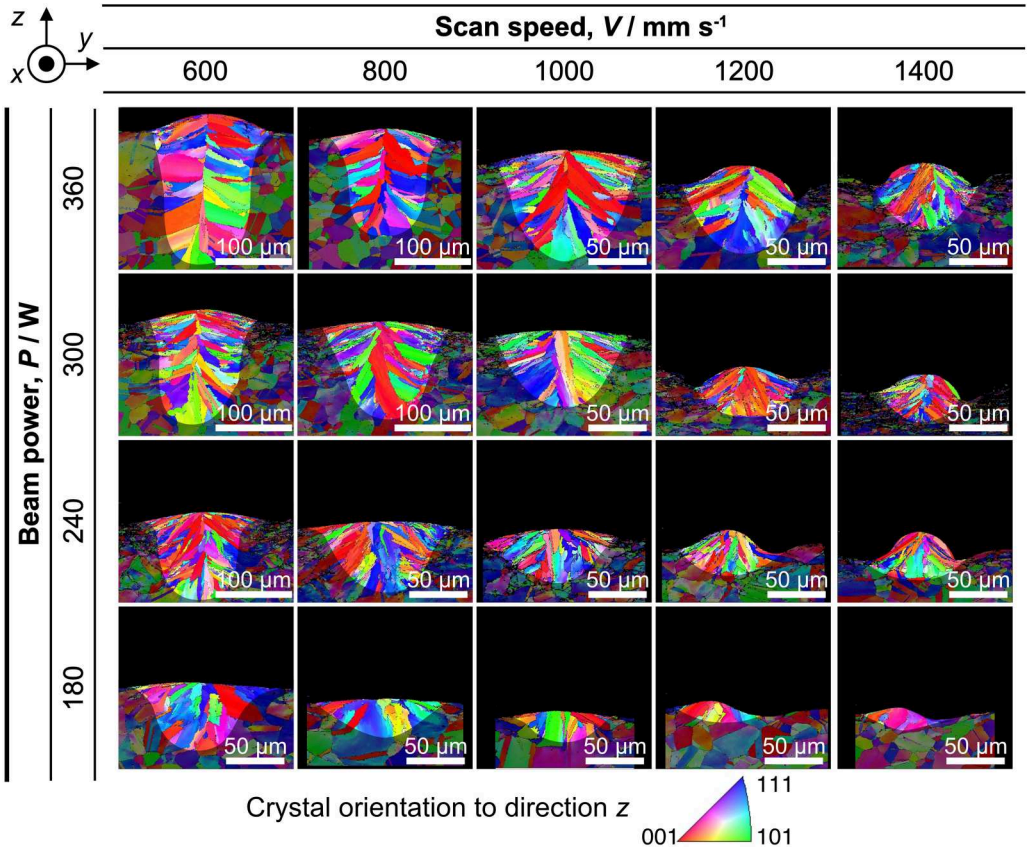

Figure 4. SEM–EBSD IPF *z* orientation maps on the transverse cross-section of the HX samples irradiated with laser beams under various beam powers *P* and scanning speeds *V*. The melt regions are indicated by bright colours while non-melted regions are represented dark shaded colours, which were confirmed with the optical images (Fig. 2b).

orientation map of the corresponding cross-section. The values of *P* and *V* were 360 W and 600 mm s^{-1}, respectively. The width and depth of the simulated melt region were in good agreement with the experimentally observed melt pools using a Fresnel coefficient of 0.12.

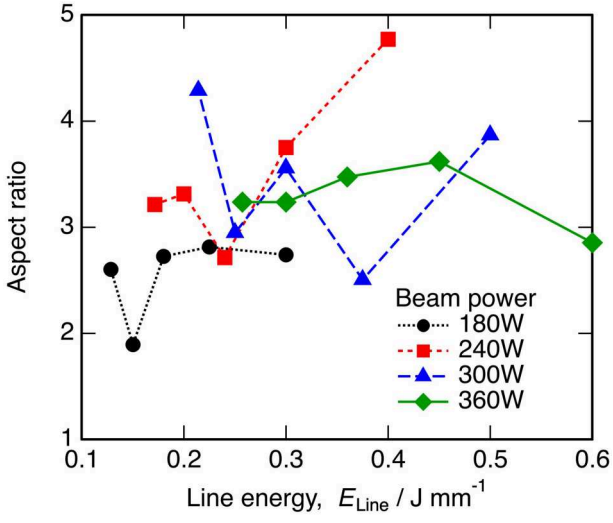

Figure 5. Average aspect ratio of laser-melted regions in the HX samples evaluated from SEM–EBSD IPF orientation maps.

The widths and depths of the simulated melt pools formed under various laser-beam irradiation conditions were measured and compared with those of the experimentally observed melt tracks, as shown in Figure 7(b1 – b3). The width, depth, and aspect ratio were consistent with the experimental results with a single Fresnel coefficient of 0.12. Although the beam absorption ratio is known to vary with temperature and surface condition, preliminary simulations using different η values indicated that a constant value of $\eta = 0.12$ can reproduce the experimentally observed melt pool dimensions across all scan conditions. Therefore, this constant absorption coefficient was adopted to approximate the thermal field and solidification conditions for microstructure analysis. Currently, simulations are conducted using a temperature-dependent absorption rate model and are compared with in situ observation data to improve the accuracy of reproducing melting and solidification behaviour.

It should be noted that there is a difference in the height between the experimentally observed melt pools and the simulated ones (Figure 7(a)). Although Marangoni convection during laser irradiation induces melt flow opposite to the scanning direction, resulting

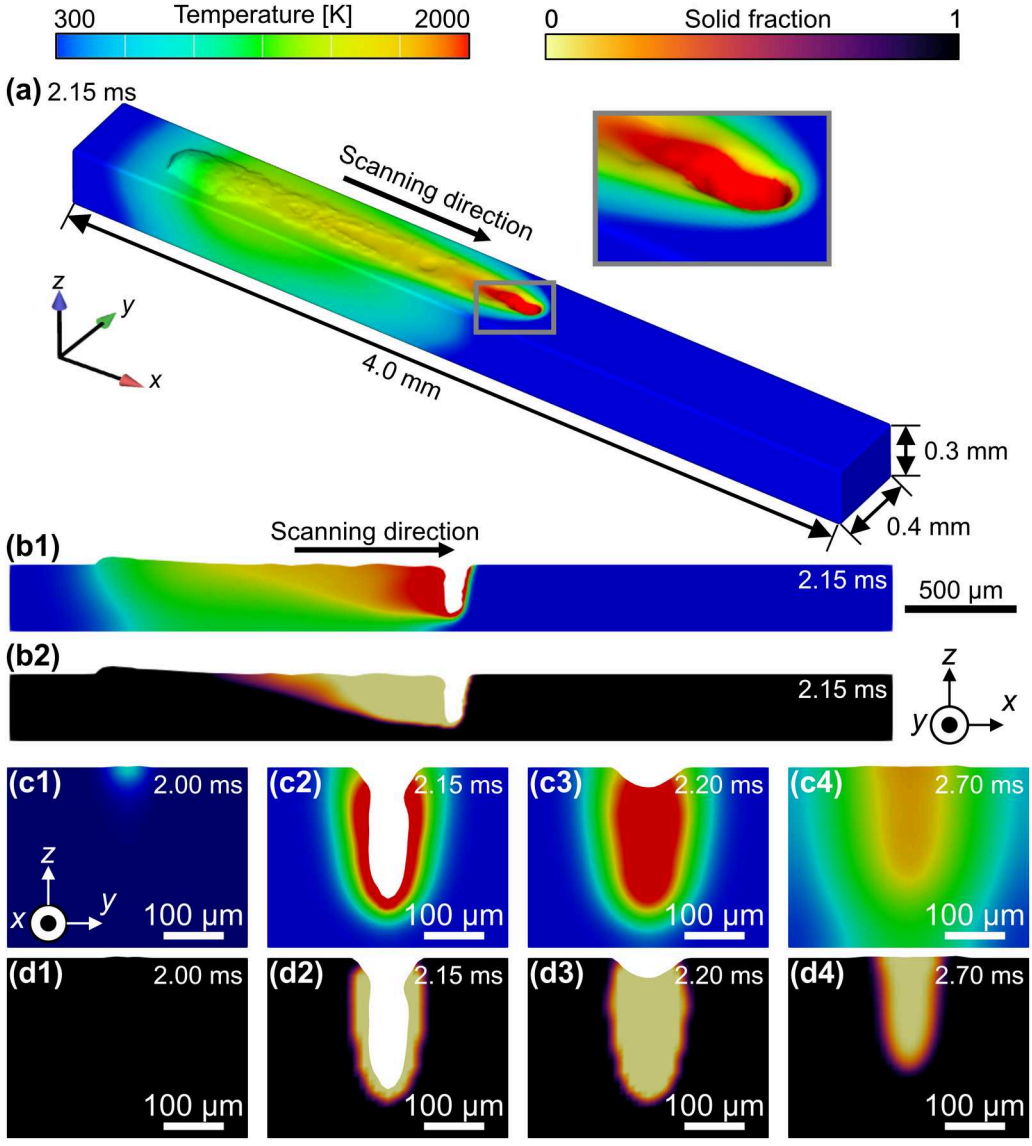

Figure 6. Snapshots of the CtFD simulation of laser beam irradiation on the HX alloy with process parameters of $P = 360$ W and $V = 600$ mm s^{-1}. (a) Bird's eye view, (b) longitudinal vertical cross-section along the centre of the scanning line, and (c1–d4) transversal vertical cross-sections at the moment of (c1, d1) 2.00 ms, (c2, d2) 2.15 ms, (c3, d3) 2.20 ms, and (c4, d4) 2.70 ms. The snapshots are coloured according to (a, b1, c1–c4) temperature or (b2, d1–d4) solid fraction.

in surface deformation, the surface profile was not used for model validation in this study. This is because the surface height depends strongly on cross-sectional location and is highly dynamic. Therefore, we focused on validating melt pool width and depth, which are more consistent and measurable. In-situ observations of melt flow and surface evolution are also currently being conducted to support future model development.

The temperature gradient (G) and solidification rate (R) were evaluated from temporal changes in the temperature distribution during the CtFD simulation. Figure 8 shows the cross-sectional views of melt pools coloured according to G (Figure 8(a)) and R (Figure 8(b)). To output the temperature conditions at the solid/liquid interface in the melt pool, only the data of the mesh with a solid phase fraction of approximately 0.5 in the CtFD simulation was plotted. It is noted that the G became extremely large at the surfaces of the melt pools. It is suggested that the surface region was cooled mainly by external thermal radiation rather than by thermal diffusion through the metal substrate. In the regions near the fusion line, the G (Figure 8(a)) was the highest, which decreased as the liquid/solid interface shifted toward the centre of the melt pool. It is noteworthy that the G became extremely large at the surface of the melt pool, suggesting that the surface region was cooled mainly by external thermal radiation rather than thermal diffusion through the

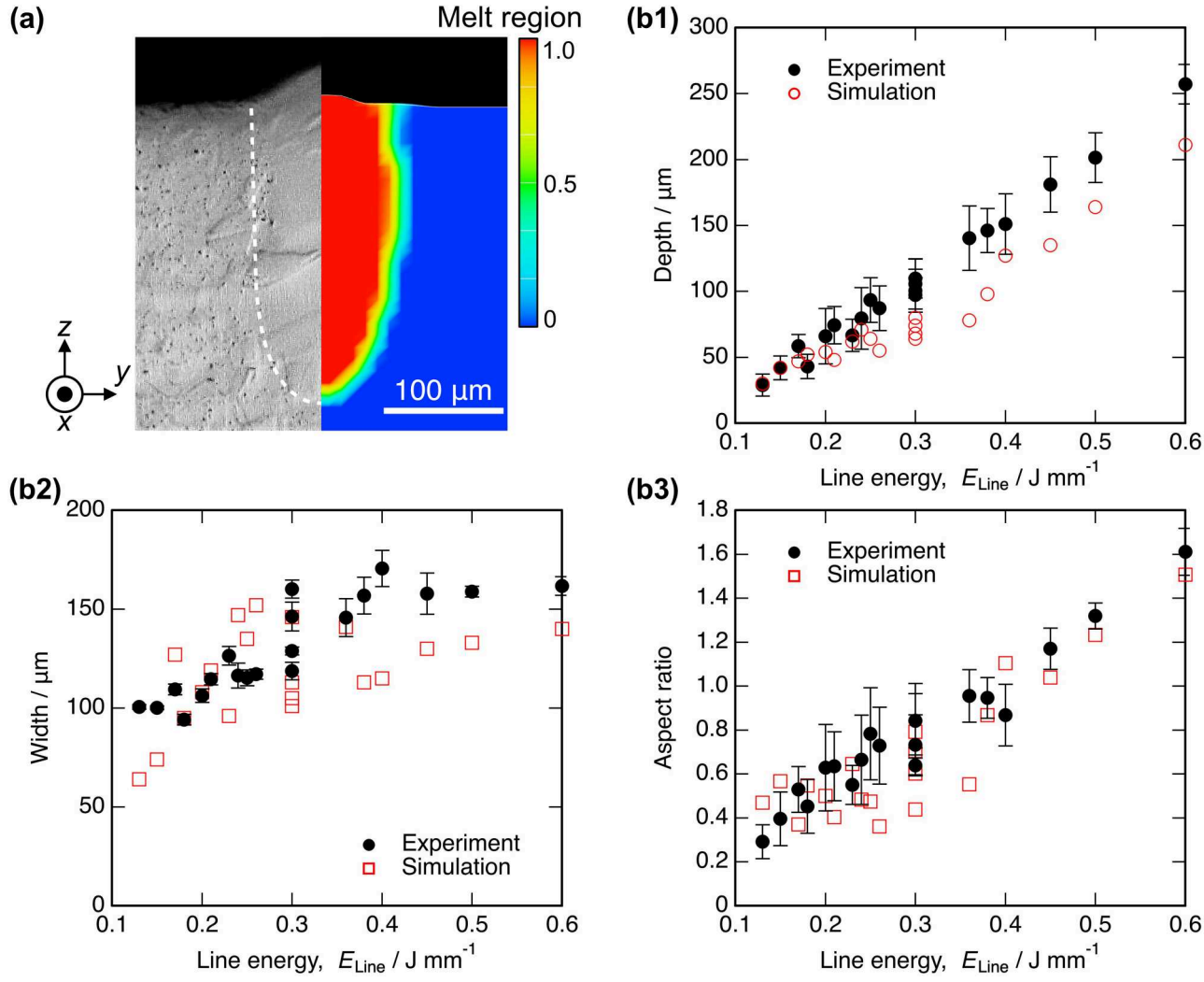

Figure 7. (a) Comparison of melt regions in experimental SEM image and CtFD simulation for the case with absorption rate of 0.8, beam power of 360 W, and beam scanning speed of 600 mm s^{-1} and (b1) depths, (b2) widths, and (b3) ratios of depth to width of CtFD simulated models plotted by line energy. For comparison, the experimental values are also presented.

metal substrate. On the other hand, the R (Figure 8(b)) was the lowest near the fusion line and increased as the interface approached the centre of the melt region.

Figure 9 shows the plots in the G – R space of the solidification conditions of each mesh coloured according to line energies (Figure 9(a)), beam powers (Figure 9(b)), and scanning speeds (Figure 9(c)). An increase in the line energy (Figure 9(a)) and scanning speed decreased both G and R, while changes in the beam power had no effect on G and R. Except for the surface regions, all the regions had G and R in the ranges of 1.0×10^5–2.0×10^8 K m^{-1} and 1.0×10^{-3}–4.0×10^0 m s^{-1}, respectively. Almost all of the conditions are out of the range of black squares in Figure 9**,** which correspond to the solidification conditions assumed for the conventional solidification map [21]. Ding et al. [29] reported that the Ni-based superalloy IN718 melted by electron beam irradiation for the PBF process at room temperature could be solidified at G and R of 10^6–10^7 K m^{-1} and 10^{-2}–10^{-1} m s^{-1}, respectively. The reported solidification conditions fell within the range of the solidification conditions obtained in this study. This study suggests that Ni-based superalloys solidify under nearly identical conditions in the PBF-type AM process, regardless of the heat source.

Figure 10 shows cross-sectional views of melt pools coloured according to the fluid flow velocity (U) of the mesh with a solid phase fraction of approximately 0.5 in the CtFD simulation. The side edges of the melt pool were solidified under high U conditions, that is, at U above 300 mm s^{-1}. In addition, the bottom regions of the melt pool melted by a beam with high line energy were solidified under high U conditions. Figure 11 shows the G – R plot coloured according to flow velocity when a liquid/solid interface passes through the mesh. Solidifications under

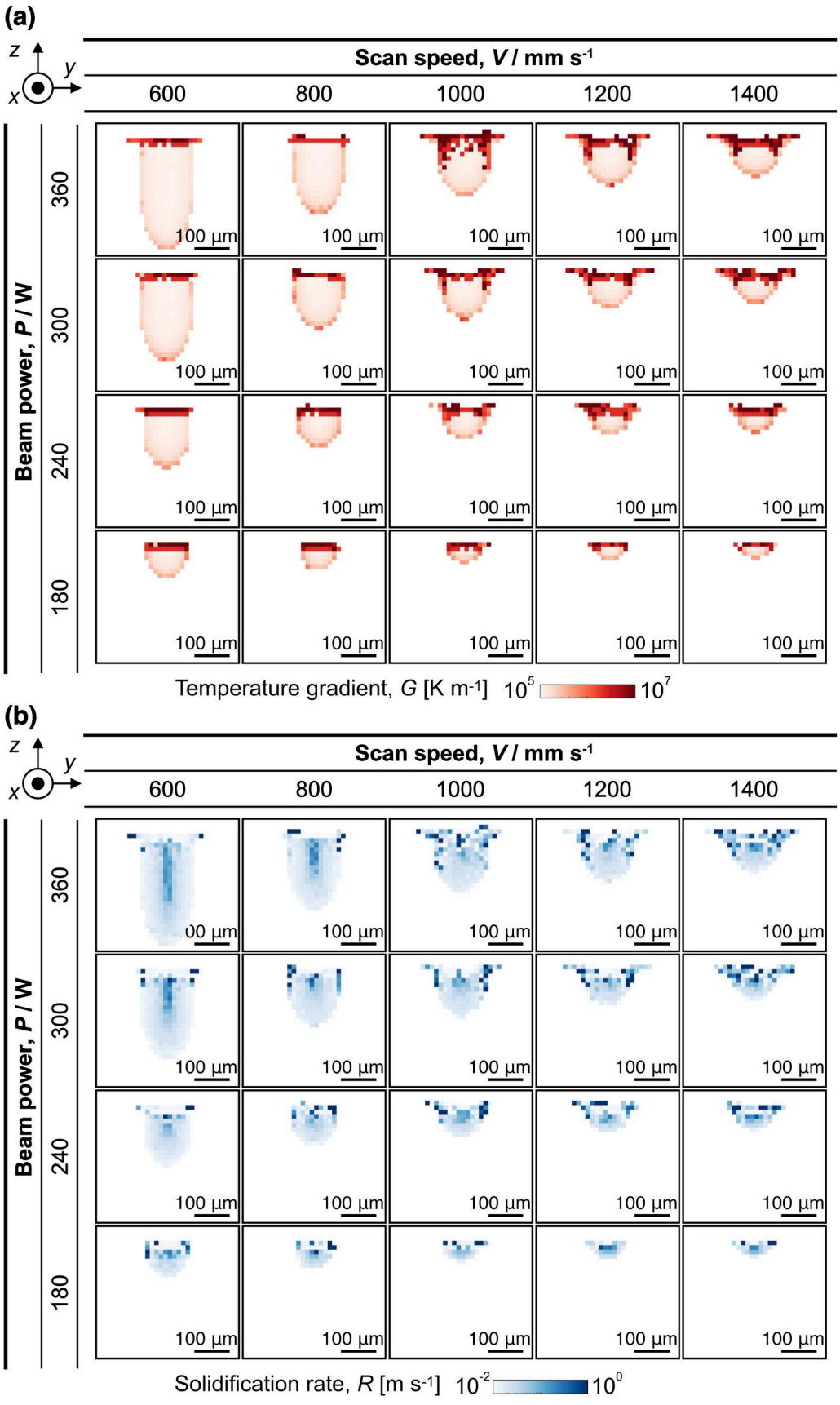

Figure 8. Cross-sectional views of melt pools of HX, simulated via CtFD, demonstrating variations in (a) temperature gradient *G* and (b) solidification rate *R* for different combinations of beam power and scan speed.

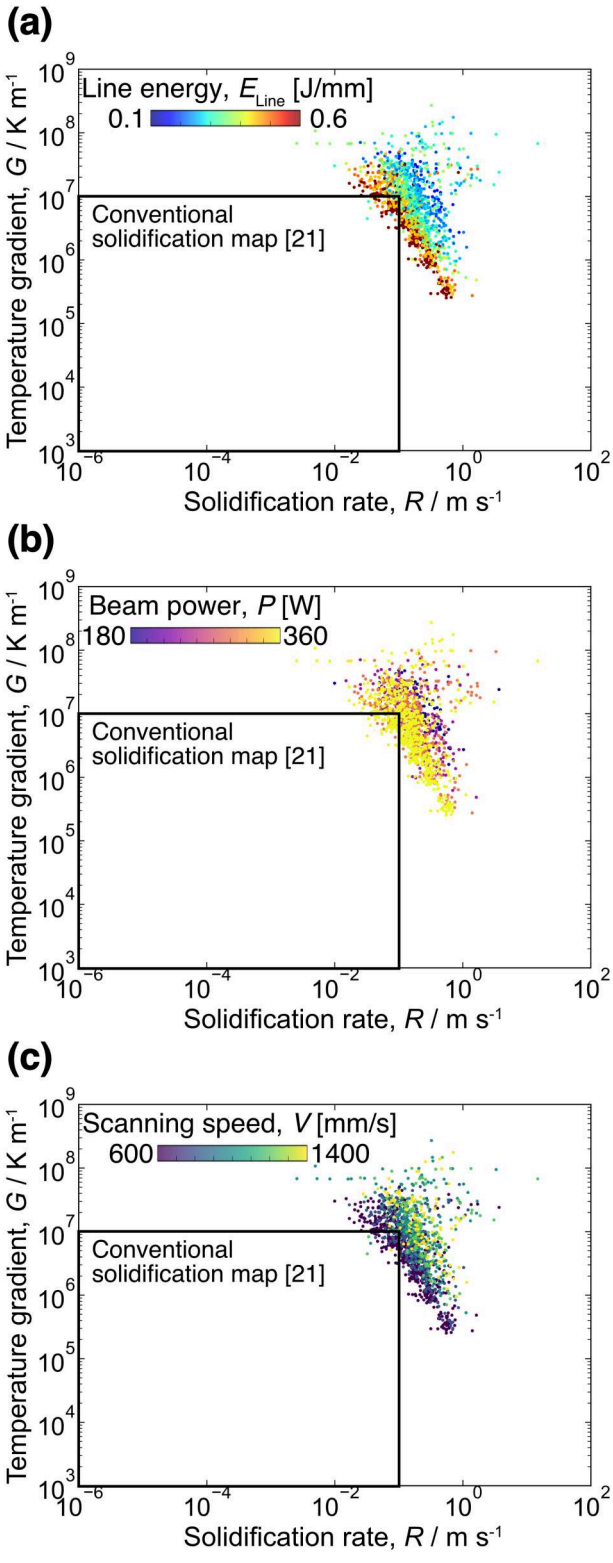

Figure 9. *G*–*R* plots of HX coloured according to (a) line energy, (b) beam power, and (c) scanning speed. Black squares indicate the ranges of solidification conditions assumed in the conventional solidification map [21].

high flow velocity conditions appeared at high *G* and *R*, suggesting that a higher cooling rate ($= G \times R$) causes a higher flow velocity.

Previous studies on the melting and solidification behaviour of stainless steels [27] and Co – Cr–Mo alloys [28] under electron beam irradiation demonstrated that equiaxed grains appear even under high *G* and low *R* conditions. Furthermore, it was suggested that these equiaxed grains are formed due to the fragmentation of dendrites and the transportation of these fragments by the high fluid velocity of approximately 400 mm s^{-1}. On the contrary, equiaxed grains were not observed in the regions solidified even under high fluid flow velocity in the HX alloy, as shown in Figure 4 and Figure 8(c). Such columnar microstructures were also observed in the Ni-based IN718 superalloy [29] prepared through the electron-beam PBF process.

The fluid flow causes grain refinement owing to the fragmentation of primally and secondly dendrites and the transport of fragments in conventional processes [39–41], and the fragmentation mainly occurs by enhancing the fluctuation of peaks and troughs due to the Plateau–Rayleigh instability, as shown in Figure 12(a) [42]. The instability is driven by surface tension: the system attempts to minimise its surface area via heat and solute diffusion in the bulk phases. Conversely, the fragmentation is suppressed under a high cooling rate because of a shortage of the time for diffusions [42, 43]. Solidifications in the PBF process also occur under rapid cooling conditions, and inverse CET microstructure formations, i.e. fragmentations of dendrites, occurs in the stainless steels [27] and the Co-Cr-Mo alloy [28]. On the other hand, the inverse CET does not occur in Ni-based alloys [29]. We propose that the difference occurs mainly by mechanical shearing fragmentations of dendrites. Figure 11(b–d) schematically illustrates the dendrite growth in the PBF-type AM process. Fast flow affects the growing Dendrites and its dynamic pressure p_v can be calculated by $p_v = 1/2\rho v^2$ using a density of liquid phase ρ and a flow velocity v. A dynamic pressure of $3.5–4.5 \times 10^3$ Pa is caused by the fast flow of an alloy liquid, assumed with $\rho = 7.0–9.0$ g cm^{-3} and $v = 1.0$ m s^{-1}. The solid fraction at the dendrite tip is 0 and at the melt-pool boundary is 1 during the solidification (Figure 12(c)). Deformations of polycrystalline in semi-solid state highly depends on the solid fraction [44–46], and when the shape of the crystal grains is close to spherical, a small amount of liquid phase relieves the constraints between the crystal grains and the flow stress decreases rapidly [44]. In the PBF process, dendrites with nearly circular shapes are formed in the cross section perpendicular to the growth direction (Figure 12(d)). Thus, there is almost no mechanical interaction between dendrites during the deformation in the semi-solid phase, and we propose that the deformation occurs depending on

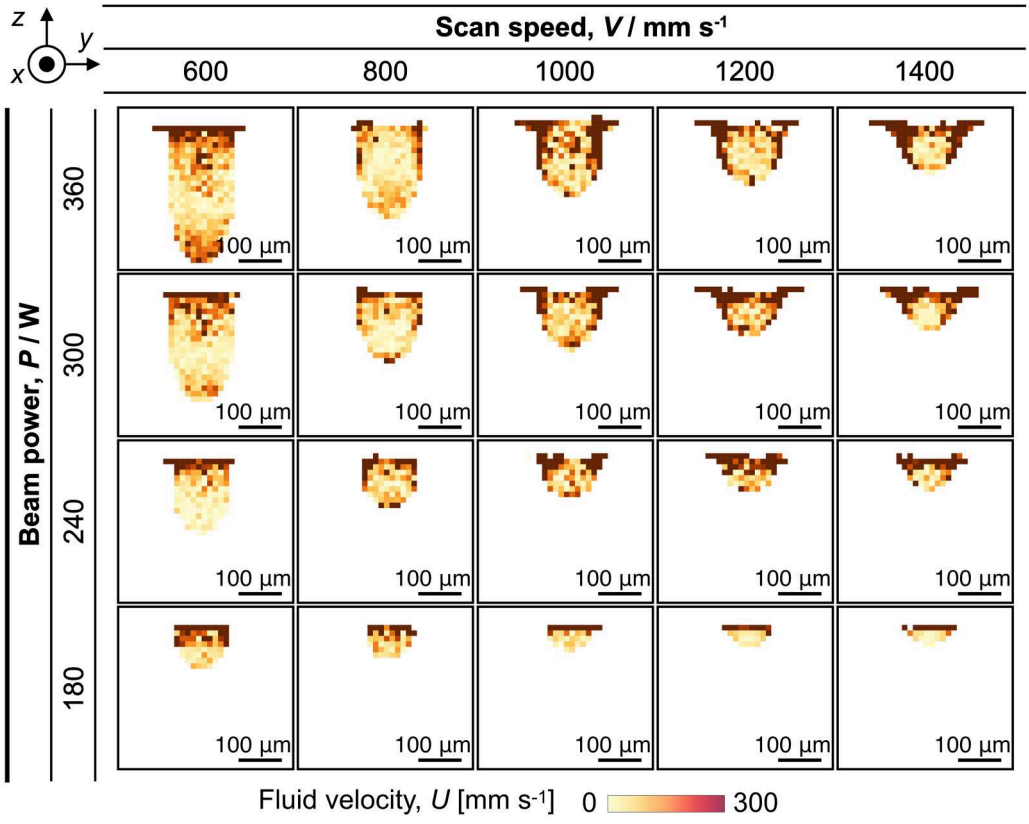

Figure 10. Cross-sectional views of melt pools of HX coloured according to fluid flow velocity (*U*), simulated by CtFD for the varying cases with four levels of beam power (*P*) and five levels of scan speed (*V*).

the strength of the dendrite itself. HX Ni-based superalloy [47] exhibits higher strengths at high temperatures than stainless steels [48] and Co alloys [49]. Therefore, it is supposed that the Ni-based superalloys are difficult to refine by fast fluid flow occurring in the PBF process and the inverse CET behaviour is not observed in the PBF process of the HX alloy in this study.

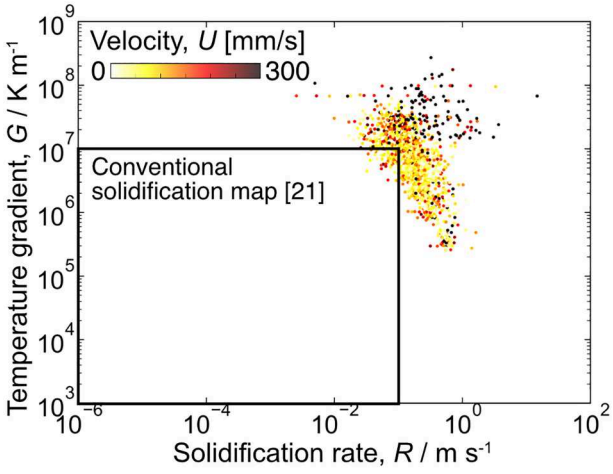

Figure 11. *G*–*R* plot of HX coloured according to *U*. Black rectangular indicates the ranges of solidification conditions assumed in the conventional solidification map [21].

However, it is necessary to investigate the fragmentation process by experiments and computational simulations, such as in-situ experimental observations of melting and solidification processes induced by laser irradiation and phase-field simulations of crystal growth that take into account the effects of fast flow.

Martin et al. [50] reported that the deep keyhole melting can lead to pore formation, and the effects of porosity or defects on the strength must be discussed. However, the process conditions, e.g. *P* and *V*, used in this study are reported [22, 31] to be able to fabricate the dense parts without defect formations. In our experiments, optical and SEM images of cross-sections did not reveal significant porosity or lack-of-fusion defects. More quantitative assessment of fragmentation and defect formation would strengthen the conclusions and in-situ observation experiments are currently underway.

3.3. Relationships between grain structures and solidification conditions

Solidification microstructures can be predicted from solidification conditions defined by the combination of a temperature gradient, *G*, and *R* at a solid/liquid interface using the CET criteria proposed by Hunt [21]: Hunt

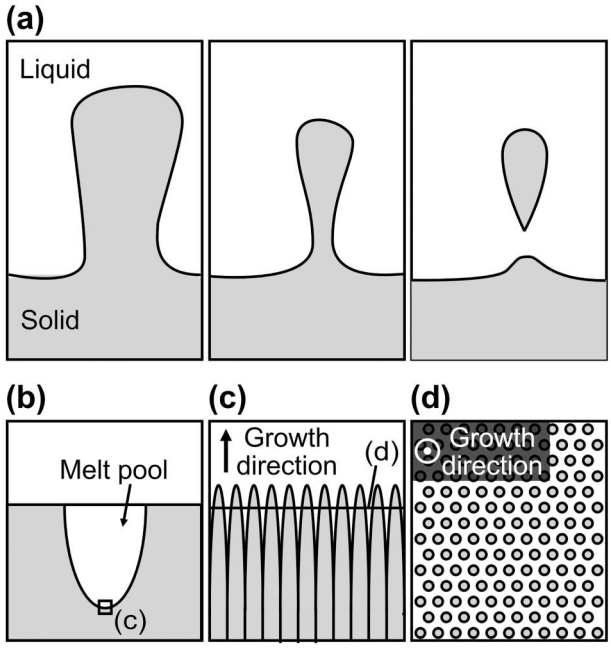

Figure 12. Schematic illustrations of (a) the fragmentation caused by enhancing the fluctuation of peaks and troughs due to the Plateau–Rayleigh instability: (a1) Initial dendrite shape before instability, (a2) growth of surface fluctuations due to the Plateau–Rayleigh instability, (a3) fragmentation of dendrites into smaller pieces; (b–d) the dendrite growth in the PBF-type AM process. (b) Melt pool geometry, (c) growth of cellular dendrites, (d) Cross-sectional view perpendicular to the growth direction (growth direction is normal to the plane of the figure).

compare an equiaxed growth and hemispherical dendrite growth, and suggested the criterion for the fully columnar microstructure:

$$G > 0.617(100N_0)^{1/3}\Delta T_c\left(1-\frac{\Delta T_n^3}{\Delta T_c^3}\right) \quad (4)$$

$$\Delta T_c = (R\cdot C_0/A)^{1/2} \quad (5)$$

Here, N_0, ΔT_c, ΔT_n, C_0, and A are the density of the heterogeneous nucleation sites, the dendrite tip undercooling, the undercooling at the heterogeneous nucleation temperature, the alloy composition, and a constant, respectively. Gäumann et al. [50, 51] modified the criterion for realistic dendrite growth models of complex alloys, such as superalloys, introducing material dependent constants a and n:

$$G > 8.6\frac{N_0^{1/3}}{n+1}\Delta T_c\left(1-\frac{\Delta T_n^{n+1}}{\Delta T^{n+1}}\right) \quad (6)$$

$$\Delta T_c = (R\cdot a)^{1/n} \quad (7)$$

Additionally, the nucleation undercooling ΔT_n is proposed to be safely neglected for solidification under high G and high R conditions [52] and the criterion can

Table 3. Parameters used for calculating the CET criteria.

Name	Symbol	IN718 [54, 55]	CMSX-4 [52]
Temperature difference between T_L and T_S	ΔT_0	76 K	66 K
Alloy constant (coefficient of proportion)	a	4.5 K^2 s m^{-1}	1.2 K^2 s m^{-1}
Alloy constant (exponent)	n	2	3.4
Density of heterogeneous nucleation sites	N_0	2.65×10^{14} m^{-3}	2×10^{15} m^{-3}

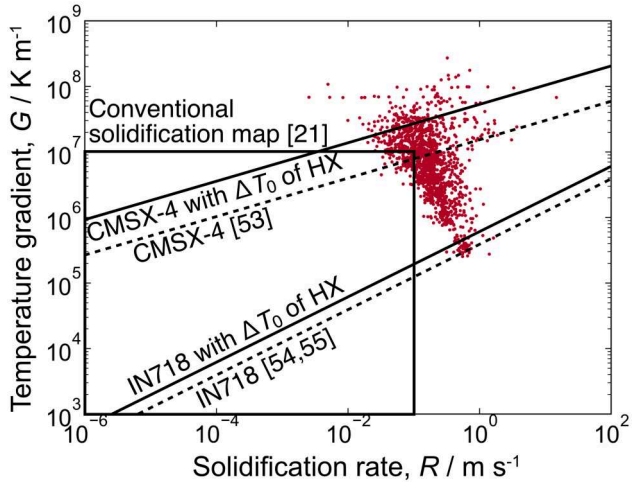

Figure 13. A comparison between solidification conditions evaluated by the CtFD simulation and CET criteria calculated using with a, n, and N_0 of IN718 and CMSX-4 shown in Table 4 (dashed lines), and ΔT_0 for the alloys and the HX alloy (solid lines). Fully columnar dendrite growth is predicted to occur under a higher G/R condition than the CET criteria.

be expressed as following:

$$\frac{G^n}{R} > a\left(8.6\Delta T_0\frac{N_0^{1/3}}{n+1}\right)^n \quad (8)$$

where ΔT_0 is the differences between the liquidus and solidus temperatures. Thus, solidification maps, in which the types of solidification microstructures are indicated in the spaces of G and R, have been proposed as a guide for predicting the microstructure formed using the PBF-type AM process.

In this study, columnar crystals were formed under almost all solidification conditions, as shown in Figure 5. Therefore, all of the solidification conditions obtained in this study were within the columnar region; that is, the solidification occurred under higher G/R conditions than those required for the CET criterion [21, 51–53] for fully columnar dendrite growth. Table 3 shows ΔT_0, a, and N_0 of the Ni-based superalloys IN718 [54, 55] and CMSX-4 [52] used for calculating the CET criteria in

Table 4. Compositions of Ni-based superalloys (mass%).

Element	Ni	Al	Co	Cr	Hf	Mo	Re	Ta	Ti	W	C	Nb	Si	Fe	Mn	P
HX	Bal.	-	1.1	21.4	-	8.8	-	-	-	0.5	0.08	-	0.39	17.6	0.46	0.01
CMSX-4	Bal.	5.6	9	0.1	0.6	3	6.5	1	6	-	-	-	-	-	-	-
IN718	Bal.	0.44	0.14	18.6	-	2.93	-	0.01	0.82	-	0.06	4.96	0.07	18.7	-	-

previous studies. Using a and N_0 of these alloys, the CET criteria for full columnar growth were calculated to predict a and N_0 of HX, as shown in Figure 13. For quantitative analysis, it is preferable to use experimentally determined CET parameters for HX. The primary aim of this study was not to establish definitive guidelines for microstructure control but rather to elucidate the trends in microstructure formation in the single-track experiment. Thus, the analysis was conducted using previously determined CET parameters for the other Ni-based superalloys. The solidification conditions of HX evaluated by CtFD calculations are also shown for comparison. Only columnar crystals form under the higher G/R condition than the line, and equiaxed crystals form under the smaller G/R condition than the line. The modified CET criteria shifted to a higher G value from the positions of the originally predicted lines because the ΔT_0 of HX (95 K) was larger than those of IN718 (76 K [54]) and CMSX-4 (66 K [52]). The CET criterion line calculated using a and N_0 of IN718 was located below the solidification condition. In contrast, the line using the values of CMSX-4 was located above the solidification condition. In this study, columnar crystals were formed under almost all conditions; therefore, the transition line predicted using the values of IN718 agreed with the experimental trend. In the solidification process, the heterogeneous nucleation ability is generally discussed based on the composition of the heterogeneous nuclei [56, 57]. It can be assumed that N_0 is almost the same as that in the alloys with similar compositions under the same solidification conditions. Table 4 lists the alloy compositions of HX, IN718, and CMSX-4, and the composition of HX is similar to that of IN718. Although further study is needed to fully understand how compositional differences, such as variations in Co and Mo content, may affect the nucleation site density N_0, we consider it reasonable to approximate the trend in microstructure morphology of HX using the N_0 value reported for IN718. This is based on the assumption that nucleation-promoting precipitates (e.g. oxides, borides, nitrides) form in a similar manner in both alloys under L-PBF conditions due to comparable levels of trace impurities. Therefore, it is suggested that that the trend in microstructure morphology of HX can be described using the values of IN718.

Although experimental determination of CET-related parameters such as N_0 would be ideal, it requires extensive effort under controlled conditions. In this study, we adopted a reference value from IN718 due to its compositional similarity with HX. This methodology provides a practical approach to predicting trends in solidification microstructure in alloys fabricated by PBF with comparable compositions. Additionally, in-situ alloying has become possible in recent years [58], and it is possible to custom-order alloy compositions easily, which is one of the advantages of the PBF process rather than other processes. We think that controlling the microstructural formation is also important for an order-made alloy [1, 4]. The advanced aspect of the present study is that it has been shown that parameters can be predicted from the composition as a guideline for controlling the microstructure.

4. Conclusions

We investigated the solidification microstructure of HX Ni-based superalloys melted through laser beam irradiation for PBF type AM process. Additionally, we evaluated the solidification conditions at the solid/liquid interface using CtFD simulations of the laser melting process. Combining the experimental and computational data, we achieved a deeper understanding of the relationship between the solidification conditions and the resulting microstructure.

The surface morphology of a single bead varied depending on the process parameters; that is, uniformly melted beads were formed through laser beam irradiation under the conditions of (1) low V and (2) high beam power and high V. On the other hand, a chain of drop-like melt tracks was formed under high-speed scanning conditions owing to Plateau-Rayleigh instability. The width of the melt pools increased and approached approximately 160 μm as the line energy increased under all the energy conditions. The depth increased monotonically as the line energy increased, regardless of the changes in P and V. EBSD analysis revealed epitaxial growth from the non-melted region under all conditions. Columnar crystals with diameters of approximately 5–10 μm appeared at the centre of the melt regions, and the morphology of the microstructures did not change significantly with the process parameters.

Keyhole mode melting was observed at the front of the melt region in the CtFD simulations. Both the width and depth of the simulated melt pools formed

under various laser beam irradiation conditions were consistent with the experimental results, with a single Fresnel coefficient of 0.12.

The temperature gradient (G), solidification rate (R), and flow velocity (U) at the solid/liquid interface in the molten pool were evaluated from the temporal changes in the temperature distribution of the CtFD simulation results. Except for the surface regions, all the regions exist under conditions of G in the range of 1.0×10^5–2.0×10^8 K m^{-1} and R in the range of 1.0×10^{-3}–4.0×10^0 m s^{-1}. G was highest in the regions near the fusion line (melt-pool boundary) and decreased as the liquid/solid interface moved toward the centre of the melt pool. On the other hand, R is lowest near the fusion line and increases as the interface approaches the centre of the melt region.

Columnar crystals were formed under almost all the solidification conditions. The microstructural morphology of HX is within the range predicted to be columnar by the CET criterion using a and N_0 of IN718 and ΔT_0 of HX (95 K). The number of heterogeneous nucleation sites was assumed to be almost the same as those in the alloys with similar compositions under the same solidification conditions. Therefore, the trend in microstructure morphology of HX can be described using the values of IN718, whose alloy composition is similar to that of HX. Further validation focuses on experimentally determining the CET parameters (ΔT_0, a, n, and N_0) of HX and on validating the criteria across various scanning strategies and multi-layer build processing conditions to confirm the applicability of the findings.

Acknowledgments

We would like to thank Mr. H. Kawabata and Mr. K. Kimura for their technical support in the sample preparation and laser beam irradiation experiments.

Author contributions

Masayuki Okugawa: Conceptualization, Formal analysis, Investigation, Methodology, Software, Visualization, Writing – original draft, Writing – review & editing; **Haruki Yoshima:** Formal analysis, Investigation, Methodology, Software, Visualization, Writing – original draft; **Yuheng Liu:** Validation, Writing – review & editing; **Pan Wang:** Validation, Writing – review & editing; **Yuichiro Koizumi:** Conceptualization, Formal analysis, Funding acquisition, Investigation, Methodology, Project administration, Supervision, Writing – review & editing; **Takayoshi Nakano:** Funding acquisition, Project administration, Supervision, Writing – review & editing.

Disclosure statement

No potential conflict of interest was reported by the author(s).

Funding

This work was partly supported by the Cabinet Office, Government of Japan, Cross-ministerial Strategic Innovation Promotion Program (SIP), 'Materials Integration for Revolutionary De-sign System of Structural Materials' (funding agency: The Japan Science and Technology Agency), JSPS KAKENHI Grant Numbers 21H05018 and 21H05193, and CREST Nanomechanics: Elucidation of macroscale mechanical properties based on understanding nanoscale dynamics for innovative mechanical materials (Grant Number: JP-MJCR2194) from the Japan Science and Technology Agency.

ORCID

Masayuki Okugawa http://orcid.org/0000-0002-6844-6856
Yuheng Liu http://orcid.org/0000-0003-1790-1844
Pan Wang http://orcid.org/0000-0002-2079-9580
Yuichiro Koizumi http://orcid.org/0000-0001-7061-7135
Takayoshi Nakano http://orcid.org/0000-0001-8052-1698

Data availability statement

The data that support the findings of this study are openly available in Mendeley Data at http://doi.org/10.17632/7cgzv6dggj.1.

References

[1] Hagihara K, Nakano T. Control of anisotropic crystallographic texture in powder Bed fusion additive manufacturing of metals and ceramics—A review. Jom. 2022;74:1760–1773. doi:10.1007/s11837-021-04966-7
[2] Okugawa M, Isono Y, Koizumi Y, et al. Raking process for powder bed fusion of Ti–6Al–4V alloy powder analyzed by discrete element method. Mat Trans. 2023;64:37–43. doi:10.2320/matertrans.MT-MLA2022010
[3] Koizumi Y, Okugawa M. Digital twin science of metal powder bed fusion additive manufacturing: a selective review of simulations for integrated computational materials engineering and science. ISIJ Int. 2022;62:2183), doi:10.2355/isijinternational.ISIJINT-2022-184
[4] Ishimoto T, Morita N, Ozasa R, et al. Superimpositional design of crystallographic textures and macroscopic shapes via metal additive manufacturing—game-change in component design. Acta Mater. 2025;286:120709. doi:10.1016/j.actamat.2025.120709
[5] Raghavan N, Dehoff R, Pannala S, et al. Numerical modeling of heat-transfer and the influence of process parameters on tailoring the grain morphology of IN718 in electron beam additive manufacturing. Acta Mater. 2016;112:303–314. doi:10.1016/j.actamat.2016.03.063
[6] Raghavan N, Simunovic S, Dehoff R, et al. Localized melt-scan strategy for site specific control of grain size and primary dendrite arm spacing in electron beam additive manufacturing. Acta Mater. 2017;140:375–387. doi:10.1016/j.actamat.2017.08.038
[7] Wang P, Ng FL, Nai MLS, et al. Towards the mechanism of in situ welding during electron beam powder bed fusion

process. Mat Sci Eng A. 2022;858:144170. doi:10.1016/j.msea.2022.144170
[8] Keller T, Lindwall G, Ghosh S, et al. Application of finite element, phase-field, and CALPHAD-based methods to additive manufacturing of Ni-based superalloys. Acta Mater. 2017;139:244. doi:10.1016/j.actamat.2017.05.003
[9] Zhang F, Levine LE, Allen AJ, et al. Effect of heat treatment on the microstructural evolution of a nickel-based superalloy additive-manufactured by laser powder bed fusion. Acta Mater. 2018;152:200–214. doi:10.1016/j.actamat.2018.03.017
[10] Harrison NJ, Todd I, Mumtaz K. Reduction of micro-cracking in nickel superalloys processed by selective laser melting: A fundamental alloy design approach. Acta Mater. 2015;94:59–68. doi:10.1016/j.actamat.2015.04.035
[11] Wang H, Chen L, Dovgyy B, et al. Micro-cracking, microstructure and mechanical properties of hastelloy-X alloy printed by laser powder bed fusion: As-built, annealed and hot-isostatic pressed. Add Manuf. 2021;39:101853. doi:10.1016/j.addma.2021.101853
[12] Tomus D, Rometsch PA, Heilmaier M, et al. Effect of minor alloying elements on crack-formation characteristics of hastelloy-X manufactured by selective laser melting. Add Manuf. 2017;16:65–72. doi:10.1016/j.addma.2017.05.006
[13] Kitano H, Tsujii M, Kusano M, et al. Effect of plastic strain on the solidification cracking of hastelloy-X in the selective laser melting process. Add Manuf. 2021;37:101742. doi:10.1016/j.addma.2020.101742
[14] Okugawa M, Izumikawa D, Koizumi Y. Simulations of non-equilibrium and equilibrium segregation in nickel-based superalloy using modified scheilgulliver and phase-field methods. Mat Trans. 2020;61:2072–2078. doi:10.2320/matertrans.MT-MA2020005
[15] Okugawa M, Saito K, Yoshima H, et al. Solute segregation in a rapidly solidified hastelloy-X Ni-based superalloy during laser powder bed fusion investigated by phase-field and computational thermal-fluid dynamics simulations. Add Manuf. 2024;84:104079. doi:10.1016/j.addma.2024.104079
[16] Xu J, Gruber H, Deng D, et al. Short-term creep behavior of an additive manufactured non-weldable nickel-base superalloy evaluated by slow strain rate testing. Acta Mater. 2019;179:142–157. doi:10.1016/j.actamat.2019.08.034
[17] Kontis P, Chauvet E, Peng Z, et al. Atomic-scale grain boundary engineering to overcome hot-cracking in additively-manufactured superalloys. Acta Mater. 2019;177:209–221. doi:10.1016/j.actamat.2019.07.041
[18] Ramsperger M, Singer RF, Körner C. Microstructure of the nickel-base superalloy CMSX-4 fabricated by selective electron beam melting. Met Mat Trans A. 2016;47:1469–1480. doi:10.1007/s11661-015-3300-y
[19] Körner C, Ramsperger M, Meid C, et al. Microstructure and mechanical properties of CMSX-4 single crystals prepared by additive manufacturing. Met Mat Trans A 2018;49:3781–3792. doi:10.1007/s11661-018-4762-5
[20] Tang YT, Panwisawas C, Ghoussoub JN, et al. Alloys-by-design: application to new superalloys for additive manufacturing. Acta Mater. 2021;202:417–436. doi:10.1016/j.actamat.2020.09.023
[21] Hunt JDD. Steady state columnar and equiaxed growth of dendrites and eutectic. Mat Sci Eng. 1984;65:75–83. doi:10.1016/0025-5416(84)90201-5
[22] Hibino S, Todo T, Ishimoto T, et al. Control of crystallographic texture and mechanical properties of hastelloy-X via laser powder bed fusion. Crystals (Basel). 2021;11:1064–1012. doi:10.3390/cryst11091064
[23] Karayagiz K, Johnson L, Seede R, et al. Finite interface dissipation phase field modeling of Ni–Nb under additive manufacturing conditions. Acta Mater. 2020;185:320–339. doi:10.1016/j.actamat.2019.11.057
[24] Okugawa M, Ohigashi Y, Furishiro Y, et al. Equiaxed grain formation by intrinsic heterogeneous nucleation via rapid heating and cooling in additive manufacturing of aluminum-silicon hypoeutectic alloy. J Alloys Compounds. 2022;919:165812. doi:10.1016/j.jallcom.2022.165812
[25] Okugawa M, Furushiro Y, Koizumi Y. Effect of rapid heating and cooling conditions on microstructure formation in powder Bed fusion of Al-Si hypoeutectic alloy: A phase-field study. Materials (Basel). 2022;15:6092. doi:10.3390/ma15176092
[26] Liu Y, Nose K, Okugawa M, et al. Fabrication and process monitoring of 316L stainless steel by laser powder Bed fusion with μ-helix scanning strategy and narrow scanning line intervals. Mat Trans. 2023;64:1135–1142. doi:10.2320/matertrans.mt-me2022006
[27] Miyata Y, Okugawa M, Koizumi Y, et al. Inverse columnar-equiaxed transition (CET) in 304 and 316L stainless steels melt by electron beam for additive manufacturing (AM). Crystals (Basel). 2021;11:856), doi:10.3390/cryst11080856
[28] Zhao Y, Koizumi Y, Aoyagi K, et al. Molten pool behavior and effect of fluid flow on solidification conditions in selective electron beam melting (SEBM) of a biomedical Co-Cr-Mo alloy. Add Manuf. 2019;26:202–214. doi:10.1016/j.addma.2018.12.002
[29] Ding X, Koizumi Y, Wei D, et al. Effect of process parameters on melt pool geometry and microstructure development for electron beam melting of IN718: A systematic single bead analysis study. Add Manuf. 2019;26:215–226. doi:10.1016/j.addma.2018.12.018
[30] Mino S, Okugawa M, Nakano T, et al. Raking and fusing behaviors during fabrication of multiple-layers in powder Bed fusion: an integrated discrete element and computational thermal fluid dynamics study. J Soc Powder Powder Met. 2025;72:S1465. doi:10.2497/jjspm.16P-T6-11
[31] Gokcekaya O, Ishimoto T, Hibino S, et al. Unique crystallographic texture formation in inconel 718 by laser powder bed fusion and its effect on mechanical anisotropy. Acta Mat. 2021;212:116876. doi:10.1016/j.actamat.2021.116876
[32] Anderson JD. Computational fluid dynamics. Prog Comput Fluid Dyn. Int. J. 2009;15–51. doi:10.1007/978-3-540-85056-4
[33] Hirt C, Nichols B. Volume of fluid (VOF) method for the dynamics of free boundaries. J Comp Phys. 1981;39:201–225. doi:10.1016/0021-9991(81)90145-5
[34] FlowScience. FLOW-3D | Highly-Accurate CFD Software, Free Surface Transient Flows, (2015) (accessed August 7, 2025), https://www.flow3d.com/products/flow-3d/.
[35] Tang C, Tan JL, Wong CH. A numerical investigation on the physical mechanisms of single track defects in

selective laser melting. Int J Heat Mass Transfer. 2018;126:957–968. doi:10.1016/j.ijheatmasstransfer.2018.06.073

[36] Technical Data for Nickel. Available online: https://periodictable.com/Elements/028/data.html (accessed on 16 January 2023).

[37] Guo C, Xu Z, Zhou Y, et al. Single-track investigation of IN738LC superalloy fabricated by laser powder bed fusion: track morphology, bead characteristics and part quality. J Mat Proc Technol. 2021;290:117000. doi:10.1016/j.jmatprotec.2020.117000

[38] Messler RW. Principles of Welding: Processes, Physics, Chemistry, and Metallurgy, (1999), doi:10.1242/dev.054080

[39] Hellawell A, Liu S, Lu SZ. Dendrite fragmentation and the effects of fluid flow in castings. JOM. 1997;49:18–20. doi:10.1007/BF02914650

[40] Campanella T, Charbon C, Rappaz M. Grain refinement induced by electromagnetic stirring: A dendrite fragmentation criterion. Met Mat Trans A. 2004;35:3201–3210. doi:10.1007/s11661-004-0064-1

[41] Zhang Z, Wang C, Koe B, et al. Synchrotron X-ray imaging and ultrafast tomography in situ study of the fragmentation and growth dynamics of dendritic microstructures in solidification under ultrasound. Acta Mater. 2021;209:116796. doi:10.1016/j.actamat.2021.116796

[42] Schwarz M, Karma A, Eckler K, et al. Physical mechanism of grain refinement in solidification of undercooled melts. Phys Rev Lett. 1994;73:1380–1383. doi:10.1103/PhysRevLett.73.1380

[43] Mullis AM, Haque N. Evidence for dendritic fragmentation in as-solidified samples of deeply undercooled melts. J Crystal Growth. 2020;529:125276, doi:10.1016/j.jcrysgro.2019.125276

[44] Kiuchi M, Yanagimoto J, Yokobayashi H. Flow stress, yield criterion and constitutive equation of mushy/semi -solid alloys. CIRP Ann. 2001;50:157–160. doi:10.1016/S0007-8506(07)62094-0

[45] Su TC, O'Sullivan C, Nagira T, et al. Semi-solid deformation of Al-Cu alloys: A quantitative comparison between real-time imaging and coupled LBM-DEM simulations. Acta Mater. 2019;163:208–225. doi:10.1016/j.actamat.2018.10.006

[46] Ji S, Wang K, Dong X. An overview on the process development and the formation of Non-dendritic microstructure in semi-solid processing of metallic materials. Crystals (Basel). 2022;12:1044. doi:10.3390/cryst12081044

[47] Kim WG, Yin SN, Ryu WS, et al. Tension and creep design stress-es of the "hastelloy-X" alloy for high-temperature gas cooled reactors. Mat Sci Eng A. 2008;483-484:495–497. doi:10.1016/j.msea.2006.12.184

[48] Desu RK, Krishnamurthy HN, Balu A, et al. Mechanical properties of austenitic stainless steel 304L and 316L at elevated temperatures. J Mat Res Technol. 2016;5:13–20. doi:10.1016/j.jmrt.2015.04.001

[49] Gu YF, Harada H, Ro Y. Chromium and chromium-based alloys: problems and possibilities for high-temperature service. JOM. 2004;56:28–33. doi:10.1007/s11837-004-0197-0

[50] Martin AA, Calta NP, Khairallah SA, et al. Dynamics of pore formation during laser powder bed fusion additive manufacturing. Nat Comm. 2019;10:1–10. doi:10.1038/s41467-019-10009-2

[51] Gäumann M, Bezençon C, Canalis P, et al. Single-crystal laser deposition of superalloys: processing-microstructure maps. Acta Mater. 2001;49:1051–1062. doi:10.1016/S1359-6454(00)00367-0

[52] Gäumann M, Trivedi R, Kurz W. Nucleation ahead of the advancing interface in directional solidification. Mat Sci Eng A. 1997;226-228:763–769. doi:10.1016/S0921-5093(97)80081-0

[53] Kurz W, Bezençon C, Gäumann M. Columnar to equiaxed transition in solidification processing. Sci Technol Adv Mat. 2001;2:185–191. doi:10.1016/S1468-6996(01)00047-X

[54] Knapp GL, Raghavan N, Plotkowski A, et al. Experiments and simulations on solidification microstructure for inconel 718 in powder bed fusion electron beam additive manufacturing. Additive Manufacturing 2019;25:511–521. doi:10.1016/j.addma.2018.12.001

[55] Nabavizadeh SA, Eshraghi M, Felicelli SD. Three-dimensional phase field modeling of columnar to equiaxed transition in directional solidification of inconel 718 alloy. J Crystal Growth. 2020;549:125879. doi:10.1016/j.jcrysgro.2020.125879

[56] Greer AL. Grain refinement of alloys by inoculation of melts. Philos Trans A Math Phys Eng Sci and Phil Trans R Soc A. 2003;361:479–495. doi:10.1098/rsta.2002.1147

[57] Pineda DA, Martorano MA. Columnar to equiaxed transition in directional solidification of inoculated melts. Acta Mater. 2013;61:1785–1797. doi:10.1016/j.actamat.2012.12.002

[58] Kim YS, Gokcekaya O, Sato K, et al. In-situ alloying of nonequiatomic TiNbMoTaW refractory bio-high entropy alloy via laser powder bed fusion: achieving suppressed microsegregation and texture formation. Mat Design. 2025;252:113824, doi:10.1016/j.matdes.2025.113824